fig. 1

fig. 2

TABLE 2. Galaxy Spectroscopic Parameters, by Cluster

Names	R.A.	Dec.	$V_\odot$	V_{cmb}	W_{obs}	W	W_{cor}	i	$\log W_{cor}$
	$h\ m\ s$	$d\ m\ s$	$km\ s^{-1}$	$km\ s^{-1}$	$-$	$km\ s^{-1}$	$-$	$\circ$	
(1)	(2)	(3)	(4)	(5)	(6)	(7)	(8)	(9)	(10)
A168									
110868	011059.1	+001355	13241(08)	12923	368	392	376	90	2.575(22) *
110869	011103.7	+000933	13975(07)	13658	309	315	305	81	2.485(18)
110872	011112.5	+000228	13294(07)	12977	447	447	469	66	2.671(22)
110877	011158.7	+004424	12837(07)	12520	231	231	224	81	2.351(30) *
110879	011210.0	+000118	13546(07)	13230	317	323	363	58	2.560(29) *
410098	011222.5	-000801	12432(07)	12116	348	348	372	64	2.570(13)
110885	011310.9	+000406	13372(09)	13056	253	270	314	56	2.497(27)
410553	011311.1	-000151	13292(07)	12976	330	337	335	74	2.526(25) *
110887	011528.1	+000305	12504(07)	12190	267	267	280	67	2.447(17)
A397									
121137	025050.4	+154026	14436(08)	14222	312	312	298	90	2.474(26) *
120587	025148.1	+153829	10619(07)	10406	173†	149	284	31	2.453(187) *
121055	025151.8	+155234	15218(07)	15006	410	410	448	61	2.652(15) *
121143	025155.0	+155315	10448(07)	10236	141	166	164	79	2.214(40) *
121145	025224.3	+154839	11839(07)	11627	253	253	244	87	2.387(14) *
121060	025242.0	+160127	20311(07)	20100	339	343	325	82	2.512(22) *
121061	025244.7	+155320	15292(07)	15081	321	321	438	44	2.641(26) *
2406	025322.1	+153528	10144(05)	9933	447	447	505	59	2.703(15) *
120614	025345.6	+154812	10038(06)	9828	411†	390	547	44	2.738(14) *
121154	025346.7	+154446	9381(07)	9171	178	210	211	75	2.325(64) *
121157	025357.5	+154728	25151(07)	24941	254	262	244	82	2.388(35) *
120632	025401.2	+154942	9711(08)	9501	194†	173	204	55	2.309(48) *
2420	025403.0	+154702	9880(10)	9670	625†	579	561	90	2.749(16) *
121159	025417.2	+152046	10039(08)	9830	225	225	256	58	2.408(29)
120651	025439.1	+151617	10058(10)	9849	280†	255	294	57	2.468(45) *
120652	025440.7	+151440	10287(07)	10078	267	267	364	45	2.561(19) *
121080	025457.9	+152722	9518(07)	9309	202	202	289	43	2.461(59) *
121082	025506.9	+153238	9053(07)	8845	171†	147	183	51	2.263(41) *
121085	025548.3	+155320	8645(09)	8438	280	300	329	63	2.517(32) *
2453	025627.8	+155024	9067(06)	8860	390†	365	471	49	2.673(74) *
121168	025634.8	+160337	10619(07)	10413	357	357	366	71	2.563(23)
A569									

TABLE 2. (continued)

Names	R.A.	Dec.	$V_\odot$	V_{cmb}	W_{obs}	W	W_{cor}	i	$\log W_{cor}$
	h m s	d m s	$km\ s^{-1}$	$km\ s^{-1}$	–	$km\ s^{-1}$	–	°	
(1)	(2)	(3)	(4)	(5)	(6)	(7)	(8)	(9)	(10)
170022	070344.9	+485843	6212(07)	6294	227	227	293	49	2.467(33)
170433	070438.8	+490436	6261(07)	6343	160	186	235	51	2.372(43) *
170436	070458.2	+482301	6215(07)	6300	161	168	171	74	2.233(42)
170038	070459.7	+490428	6263(08)	6346	207	207	252	54	2.401(30)
170437	070504.5	+484609	18938(07)	19022	444	444	459	65	2.662(22) *
170438	070506.4	+485442	6274(07)	6357	198	248	256	71	2.409(70) *
170439	070512.3	+483731	5932(07)	6016	173	197	195	82	2.290(35) *
170440	070517.2	+483913	5296(07)	5380	170	170	246	43	2.391(34) *
170442	070525.5	+484844	5816(08)	5900	179	200	210	69	2.321(46) *
170446	070559.0	+490038	5841(07)	5925	194	194	202	70	2.306(18) *
170057	070702.5	+481823	6283(07)	6370	205	252	249	83	2.396(31) *
170060	070711.0	+490617	6006(08)	6091	251	282	288	74	2.459(34)
3724	070742.7	+481925	5919(03)	6006	401†	375	453	54	2.656(30) *
170063	070742.9	+490949	6089(08)	6174	185	192	254	48	2.406(41) *
170468	070828.7	+485431	12414(07)	12500	235	235	264	59	2.421(18) *
A1139									
200723	105515.6	+015459	11665(07)	12030	181	193	226	55	2.353(39) *
201060	105523.5	+015525	12187(07)	12552	165	185	190	69	2.279(49)
200742	105543.4	+012434	12014(07)	12379	275	284	282	76	2.450(20)
200743	105545.3	+014941	12123(07)	12488	312	315	309	78	2.490(21) *
200752	105603.2	+014112	11383(08)	11748	297	320	322	73	2.507(29)
200760	105626.8	+014049	12540(07)	12905	230	242	249	69	2.396(32)
201069	105631.3	+015219	11898(07)	12263	255	255	255	74	2.406(31) *
200763	105631.7	+012702	11681(07)	12046	316	316	338	64	2.529(14)
200765	105634.9	+013906	11855(07)	12220	207	233	270	56	2.432(31)
200788	105706.4	+014318	12186(07)	12551	238	254	289	57	2.461(21)
200799	105726.7	+015338	12776(07)	13141	214	214	233	61	2.368(27)
A1228									
6357	111759.2	+332259	10555(25)	10838	540†	514	496	90	2.696(31) *
211469	111802.2	+344603	10542(07)	10819	364	370	360	83	2.556(17)
6364	111821.0	+343716	10727(13)	11004	552	603	582	90	2.765(25) *
211475	111849.4	+342500	12906(07)	13184	268	300	299	74	2.476(29) *
211476	111852.5	+342810	10706(10)	10984	136	200	199	76	2.298(87) *

TABLE 2. (continued)

Names	R.A.	Dec.	$V_\odot$	V_{cmb}	W_{obs}	W	W_{cor}	i	log W_{cor}
	$h\ m\ s$	$d\ m\ s$	$km\ s^{-1}$	$km\ s^{-1}$	–	$km\ s^{-1}$	–	°	
(1)	(2)	(3)	(4)	(5)	(6)	(7)	(8)	(9)	(10)
211399	111954.4	+344004	10421(07)	10698	295	295	322	62	2.508(20)
211489	112013.3	+342001	10819(07)	11097	301	305	312	70	2.494(28)
211402	112019.4	+344006	10829(09)	11106	267	284	276	84	2.440(28)
211403	112029.0	+343416	10799(07)	11076	190	194	190	81	2.278(36)
211492	112029.0	+342903	10263(07)	10541	183	205	206	74	2.313(53)
211406	112043.3	+343425	10503(07)	10780	186	196	210	65	2.321(33) *
A1983									
241306	144858.8	+165402	13839(05)	14030	226†	203	196	81	2.293(20) *
240823	145004.8	+171140	12800(09)	12989	239†	203	239	55	2.378(30) *
240825	145009.0	+163307	13526(07)	13716	316	316	327	68	2.514(12)
240840	145025.6	+170139	13748(07)	13937	330	344	353	68	2.548(23) *
241298	145045.5	+172039	13600(07)	13788	278	278	279	73	2.445(19) *
240869	145052.0	+170737	13664(07)	13852	340	340	336	75	2.526(14)
240894	145117.7	+165603	13063(07)	13251	231	235	225	87	2.353(26)
A1983b									
241056	144630.9	+170222	21342(07)	21535	535	535	507	80	2.705(09) *
241294	144645.1	+172318	11330(08)	11523	259	259	250	85	2.399(25)
9538	144652.3	+171340	11239(06)	11432	604†	570	568	75	2.755(13) *
241059	144703.4	+165621	10981(23)	11174	520†	473	475	74	2.676(28) *
241061	144709.4	+164600	21064(07)	21257	754	754	764	67	2.883(18) *
241296	144713.4	+172425	11189(07)	11381	350	390	395	72	2.597(30) *
240746	144739.2	+165639	11899(15)	12091	269†	237	243	70	2.385(55) *
240747	144741.7	+171511	11254(07)	11446	398†	359	427	54	2.631(20) *
9548	144756.3	+165530	11024(09)	11216	379	430	450	67	2.653(22) *
9550	144806.5	+165706	11063(07)	11255	519†	497	493	76	2.693(11) *

†21cm data
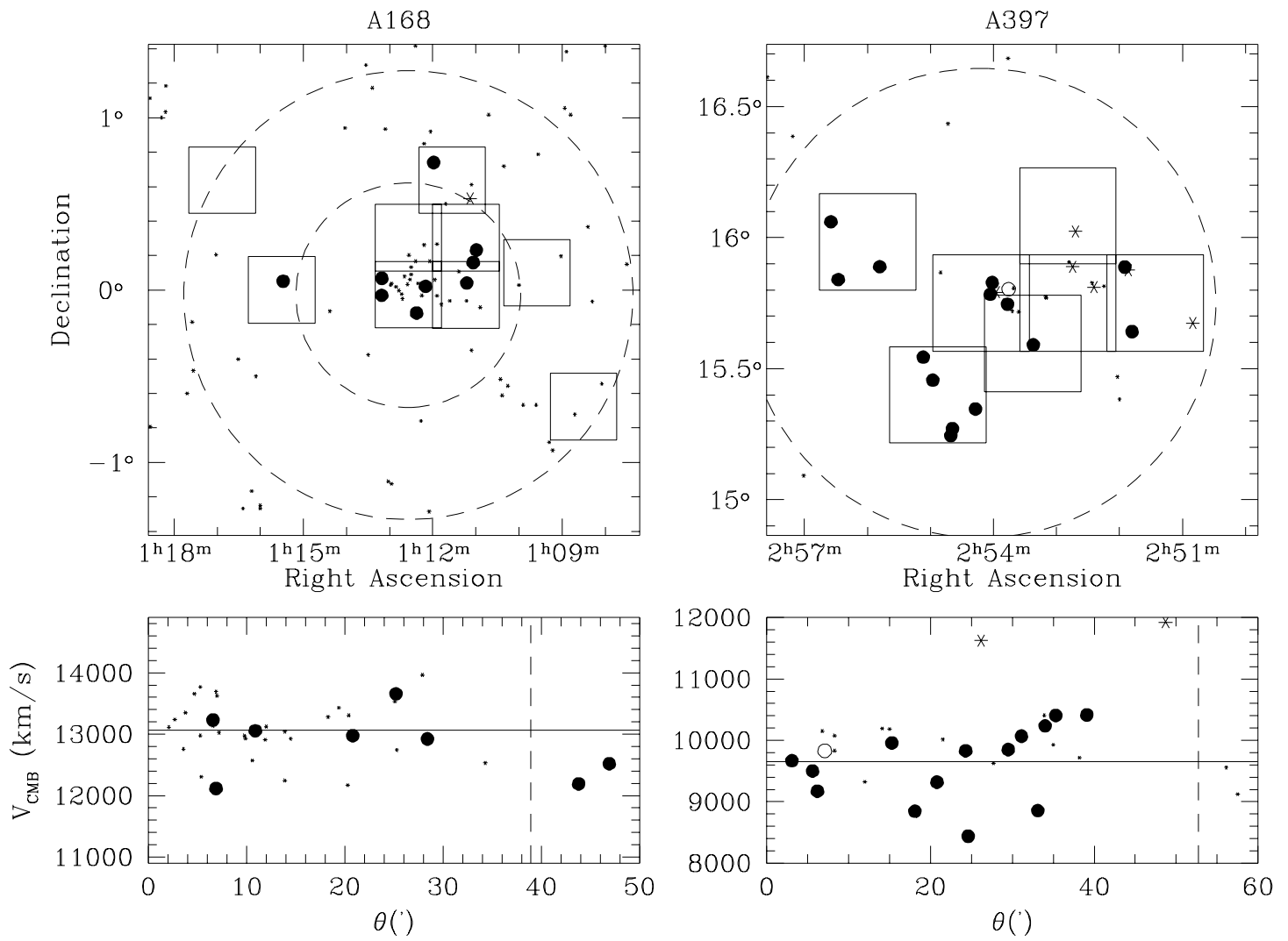
fig. 3

TABLE 3. Galaxy Photometric Parameters, by Cluster

Names	T	θ '	PA °	ϵ	ϵ_{cor}	μ_0	$R_{\rm d}$ "	R_{opt} "	$R_{23.5}$ "	$m_{23.5}$	m_∞	m_{cor}	M_{cor}
(1)	(2)	(3)	(4)	(5)	(6)	(7)	(8)	(9)	(10)	(11)	(12)	(13)	(14)
A168													
110868	1	28	87	0.755	0.806(20)	17.3	4.0	15.9	22.7	14.66	14.61	13.67	-21.91(13) *
110869	5	25	76	0.726	0.795(23)	17.3	2.8	10.8	13.4	15.78	15.70	15.05	-20.53(11)
110872	1B	21	85	0.532	0.553(69)	18.4	5.2	18.1	23.3	13.86	13.79	13.25	-22.33(08)
110877	5	47	172	0.772	0.804(14)	20.0	5.1	15.6	16.5	16.21	16.05	15.43	-20.15(10) *
110879	5	7	118	0.433	0.465(16)	17.6	2.7	12.3	15.6	14.65	14.60	14.40	-21.18(04) *
410098	3	7	120	0.495	0.528(21)	17.8	3.0	12.8	16.8	14.04	13.99	13.67	-21.91(05)
110885	7	11	3	0.395	0.424(15)	18.0	2.6	9.9	13.1	15.03	14.97	14.74	-20.84(04)
410553	5	9	1	0.645	0.703(15)	17.8	2.3	8.8	12.3	15.10	15.02	14.65	-20.93(09) *
110887	5	44	38	0.534	0.584(11)	17.8	2.8	10.8	14.6	15.08	15.02	14.65	-20.93(06)
A397													
121137	5	49	109	0.832	0.877(08)	18.6	4.2	14.1	18.2	16.02	15.94	14.88	-20.88(13) *
120587	6	35	18	0.131	0.136(63)	18.1	3.9	16.1	19.6	13.93	13.85	13.63	-21.30(05) *
121055	5	35	30	0.463	0.496(07)	17.4	2.6	13.9	17.6	14.53	14.48	14.14	-21.74(05) *
121143	5	34	38	0.687	0.769(25)	17.9	1.7	7.7	8.8	17.05	16.96	16.36	-18.57(09) *
121145	5	26	115	0.778	0.861(10)	18.2	2.1	8.0	10.4	16.74	16.68	15.79	-19.54(12) *
121060	4	27	119	0.767	0.805(08)	19.7	4.2	12.4	14.9	16.23	16.11	15.33	-21.18(12) *
121061	5	23	30	0.266	0.278(23)	19.8	4.4	12.5	14.8	14.95	14.81	14.56	-21.33(05) *
2406	1B	15	63	0.440	0.457(21)	17.5	4.9	27.5	34.4	13.30	13.24	12.60	-22.33(07) *
120614	0	7	141	0.257	0.263(04)	20.2	8.2	19.4	20.8	14.03	13.85	13.27	-21.66(06) *
121154	5	6	16	0.674	0.705(08)	20.3	4.3	11.1	12.8	16.06	15.92	15.30	-19.62(08) *
121157	5	4	104	0.731	0.807(10)	19.0	2.0	6.8	8.2	17.36	17.26	16.50	-20.48(10) *
120632	5	6	70	0.410	0.423(21)	19.6	5.8	19.0	21.0	14.59	14.44	14.07	-20.86(06) *
2420	3	3	150	0.816	0.835(10)	18.6	9.1	30.3	41.5	13.61	13.55	12.58	-22.34(15) *
121159	5	24	16	0.441	0.464(09)	19.5	3.5	9.7	12.8	15.23	15.12	14.70	-20.22(06)
120651	4B	29	67	0.430	0.447(24)	18.6	4.8	16.5	21.9	14.09	14.01	13.60	-21.33(05) *
120652	3B	31	127	0.270	0.281(12)	19.2	4.2	15.1	18.5	14.32	14.22	13.86	-21.06(05) *
121080	5	21	107	0.250	0.260(52)	19.1	4.5	15.6	18.2	14.48	14.36	14.07	-20.86(05) *
121082	5	18	140	0.357	0.365(36)	20.7	7.8	24.6	21.0	14.87	14.58	14.27	-20.65(06) *
121085	3B	25	65	0.489	0.507(26)	18.8	5.0	17.8	22.0	14.09	14.02	13.57	-21.36(06) *
2453	3B	33	128	0.320	0.325(102)	19.6	10.1	29.6	35.8	12.95	12.83	12.46	-22.46(07) *
121168	4	39	59	0.631	0.646(21)	20.0	7.6	23.6	24.4	14.67	14.49	14.02	-20.90(06)
A569													

TABLE 3. (continued)

Names	T	θ '	PA °	ϵ	ϵ_{cor}	μ_0	R_{d} "	R_{opt} "	$R_{23.5}$ "	$m_{23.5}$	m_∞	m_{cor}	M_{cor}
(1)	(2)	(3)	(4)	(5)	(6)	(7)	(8)	(9)	(10)	(11)	(12)	(13)	(14)
170022	3	23	118	0.316	0.331(16)	19.5	5.1	14.5	18.6	14.06	13.96	13.57	-20.33(05)
170433	4	24	36	0.342	0.359(28)	19.2	4.8	16.5	18.7	14.65	14.52	14.21	-19.70(04) *
170436	6	19	117	0.651	0.700(30)	18.4	3.0	12.0	14.2	15.61	15.54	15.04	-18.86(07)
170038	5	23	110	0.378	0.398(10)	18.5	4.6	16.8	20.9	14.10	14.00	13.65	-20.25(05)
170437	3	5	73	0.504	0.547(08)	18.5	3.3	12.0	18.5	14.42	14.37	13.94	-22.45(05) *
170438	3	13	108	0.612	0.627(20)	20.4	10.7	23.6	23.0	14.48	14.27	13.68	-20.22(08) *
170439	5	5	133	0.740	0.813(25)	18.1	3.1	12.7	15.3	15.88	15.79	15.15	-18.76(09) *
170440	5	3	134	0.246	0.260(21)	19.1	4.8	16.2	19.7	14.29	14.17	13.91	-19.99(04) *
170442	5	7	56	0.579	0.628(35)	19.0	3.4	12.1	14.1	15.80	15.69	15.18	-18.72(07) *
170446	5	20	61	0.596	0.641(10)	19.4	3.4	11.3	15.5	15.30	15.21	14.69	-19.21(07) *
170057	5	29	23	0.786	0.817(11)	18.7	6.3	21.6	27.8	14.56	14.46	13.69	-20.21(10) *
170060	4	30	103	0.671	0.694(11)	17.7	6.2	25.5	33.6	13.65	13.59	12.97	-20.94(08)
3724	3B	32	43	0.385	0.393(53)	18.9	9.9	32.3	41.5	12.48	12.40	12.04	-21.86(05) *
170063	6	36	160	0.307	0.320(03)	18.6	4.6	19.8	22.5	14.26	14.13	13.83	-20.07(04) *
170468	5	33	111	0.422	0.471(18)	17.6	1.7	6.2	9.3	15.28	15.25	14.85	-20.63(05) *
A1139													
200723	5	10	94	0.395	0.421(41)	19.8	3.7	11.7	12.6	15.56	15.40	15.17	-20.26(06) *
201060	5	10	163	0.575	0.625(09)	19.6	3.0	9.0	10.6	16.19	16.07	15.75	-19.68(05)
200742	3	22	114	0.624	0.685(13)	17.4	2.3	8.8	13.1	15.05	15.01	14.48	-20.96(08)
200743	3	5	158	0.648	0.719(10)	17.8	2.4	9.1	13.0	15.27	15.23	14.66	-20.78(09) *
200752	4	10	145	0.645	0.685(11)	18.9	4.3	13.5	18.0	14.98	14.91	14.55	-20.88(06)
200760	5	15	146	0.590	0.616(15)	20.1	5.2	16.5	16.0	15.83	15.61	15.24	-20.20(07)
201069	4	17	113	0.619	0.696(21)	17.6	1.9	7.1	10.2	15.76	15.72	15.21	-20.22(08) *
200763	4	24	19	0.528	0.548(06)	18.7	5.7	19.1	25.3	13.97	13.89	13.63	-21.80(04)
200765	5	18	173	0.413	0.430(16)	19.5	5.0	16.5	17.6	15.08	14.91	14.66	-20.78(05)
200788	5	24	114	0.413	0.451(06)	17.5	2.4	10.8	14.0	15.01	14.94	14.67	-20.76(05)
200799	5	30	29	0.482	0.508(20)	19.9	4.2	11.7	13.1	15.56	15.41	15.13	-20.31(05)
A1228													
6357	5	74	23	0.840	0.901(12)	14.7	3.8	24.7	32.2	13.98	13.94	12.75	-22.42(18) *
211469	3	14	69	0.705	0.763(13)	17.0	3.1	12.7	18.2	14.65	14.62	14.08	-21.09(11)
6364	2	6	96	0.804	0.835(12)	17.2	7.0	29.6	40.6	12.77	12.70	11.66	-23.51(15) *
211475	5	11	132	0.622	0.693(11)	17.8	1.9	7.1	10.2	15.74	15.71	15.23	-20.37(08) *
211476	3B	8	59	0.641	0.691(19)	17.9	2.8	11.4	14.8	14.83	14.79	14.37	-20.80(07) *

Table 3. (continued)

Names	T	θ '	PA °	ϵ	ϵ_{cor}	μ_0	R_d "	R_{opt} "	$R_{23.5}$ "	$m_{23.5}$	m_∞	m_{cor}	M_{cor}
(1)	(2)	(3)	(4)	(5)	(6)	(7)	(8)	(9)	(10)	(11)	(12)	(13)	(14)
211399	3	14	178	0.476	0.500(15)	18.9	4.4	14.5	18.0	14.71	14.61	14.32	-20.86(05)
211489	2	24	149	0.567	0.616(34)	18.4	2.7	8.7	12.6	15.13	15.08	14.40	-20.77(09)
211402	5	19	76	0.766	0.829(08)	18.3	3.1	11.1	14.6	15.75	15.69	14.97	-20.20(11)
211403	5	21	91	0.726	0.793(13)	18.6	2.7	12.5	13.6	16.42	16.30	15.82	-19.35(08)
211492	6	22	63	0.651	0.702(42)	18.0	3.0	13.1	14.4	15.85	15.74	15.29	-19.88(09)
211406	6	24	89	0.498	0.554(11)	18.9	2.0	6.5	8.5	16.23	16.15	15.85	-19.33(05) *
A1983													
241306	5	21	30	0.748	0.797(08)	19.8	3.5	10.7	11.9	16.86	16.70	16.24	-19.45(08) *
240823	5	15	36	0.380	0.410(31)	17.7	2.7	11.4	13.9	15.13	15.05	14.87	-20.82(05) *
240825	3B	24	25	0.539	0.576(07)	17.6	2.8	10.8	15.0	14.90	14.85	14.54	-21.15(05)
240840	4	5	114	0.582	0.614(13)	19.3	4.3	11.6	16.5	14.89	14.80	14.53	-21.15(05) *
241298	5	24	129	0.637	0.675(17)	20.3	3.8	10.3	10.8	16.42	16.24	15.80	-19.88(08) *
240869	2	13	152	0.644	0.680(13)	18.8	4.3	12.9	18.8	14.57	14.51	13.90	-21.78(08)
240894	5	13	41	0.802	0.862(07)	19.0	3.6	12.1	14.0	16.74	16.62	15.91	-19.78(12)
A1983b													
241056	3	13	166	0.701	0.735(11)	18.2	4.8	17.0	23.5	14.44	14.38	13.94	-22.73(11) *
241294	5	20	14	0.791	0.841(14)	18.7	3.6	13.3	16.1	16.00	15.90	15.24	-20.07(11)
9538	1	11	113	0.670	0.678(27)	20.0	16.5	33.4	48.2	12.62	12.52	11.94	-23.37(07) *
241059	1	11	51	0.637	0.662(11)	18.9	5.8	15.4	24.3	13.86	13.80	13.23	-22.08(07) *
241061	2	20	82	0.557	0.571(53)	19.7	8.7	24.8	30.5	13.58	13.46	12.94	-23.70(07) *
241296	1	19	41	0.612	0.637(52)	18.9	5.0	13.7	22.1	13.87	13.83	13.25	-22.06(08) *
240746	5	10	65	0.600	0.635(22)	19.2	3.8	12.2	14.7	15.63	15.51	15.15	-20.16(07) *
240747	2B	10	137	0.378	0.391(19)	19.2	5.5	17.4	23.9	13.62	13.55	13.11	-22.19(06) *
9548	2	13	10	0.556	0.569(29)	20.4	9.3	18.5	27.0	13.66	13.55	13.04	-22.27(07) *
9550	5	13	21	0.708	0.730(25)	17.7	7.3	26.5	37.4	13.25	13.20	12.82	-22.48(11) *
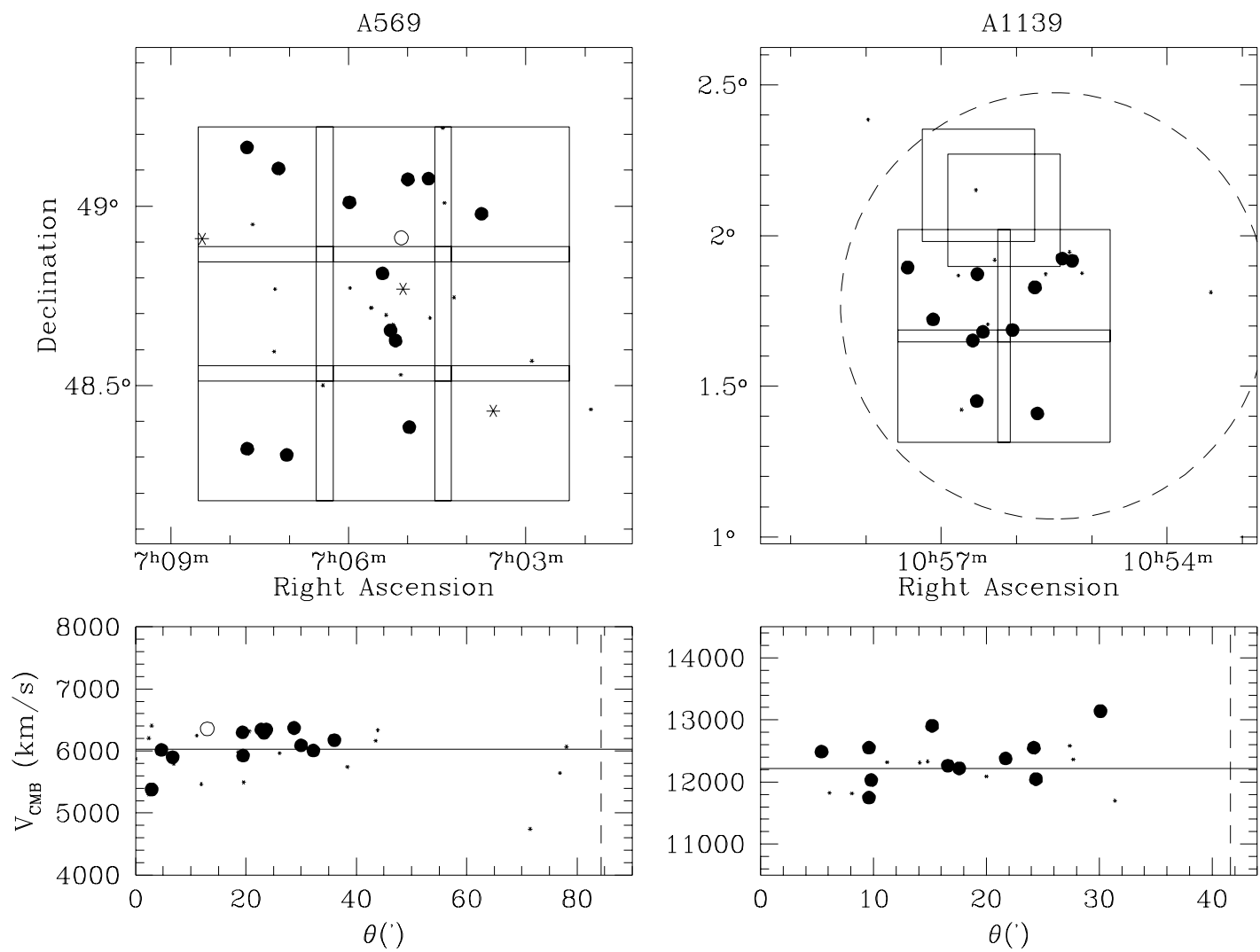
fig. 4
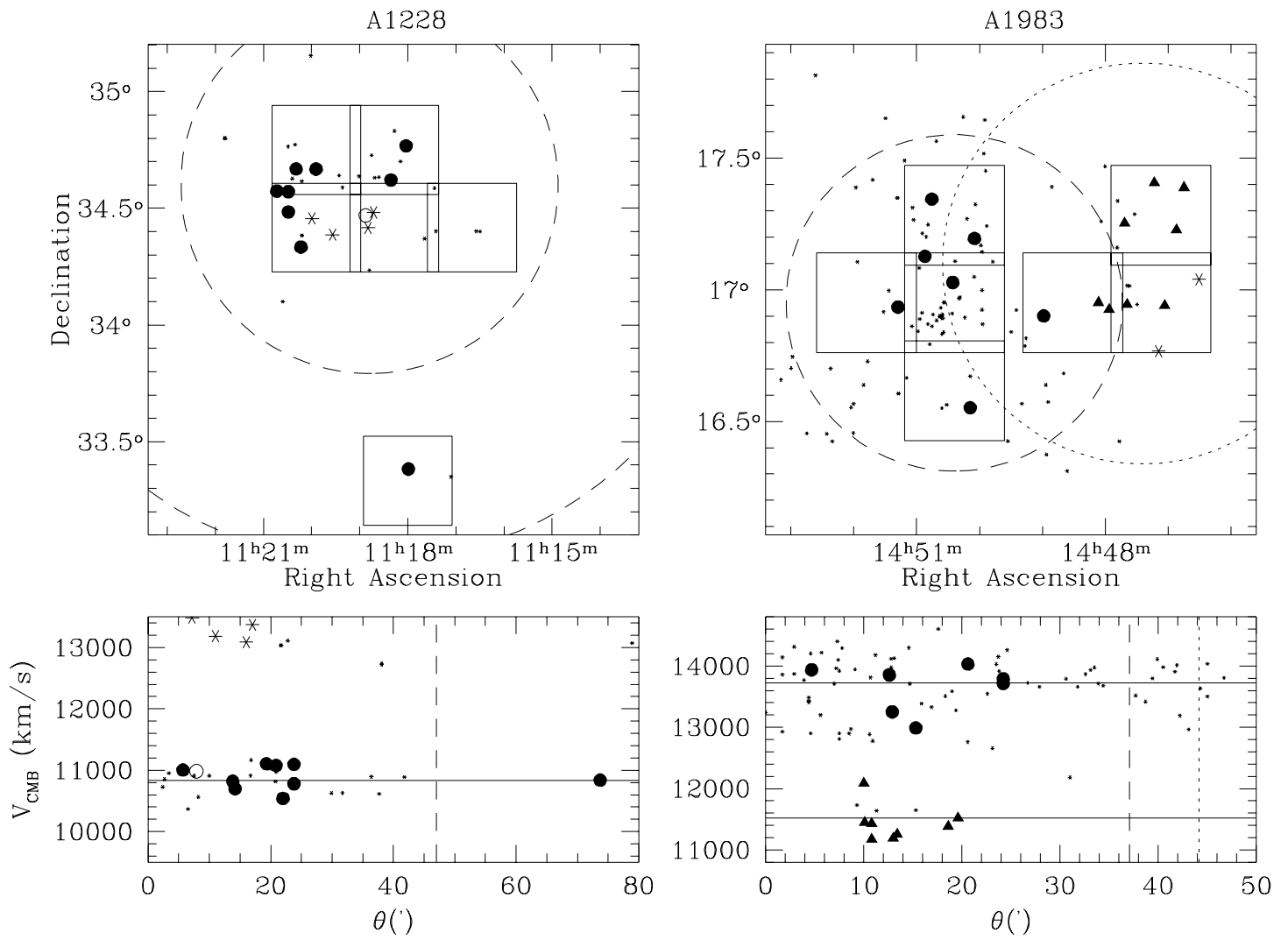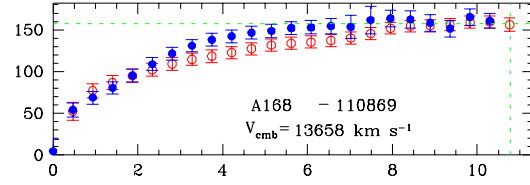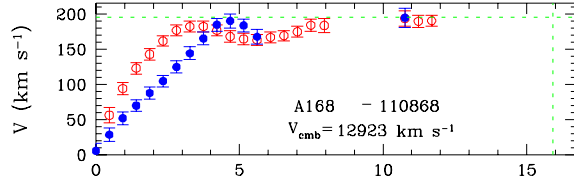
fig. 5
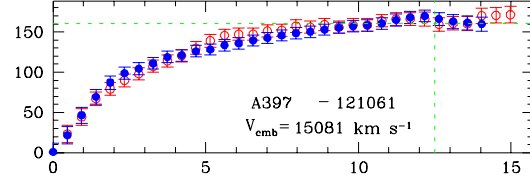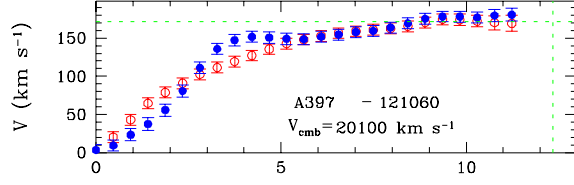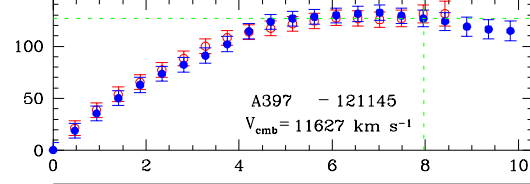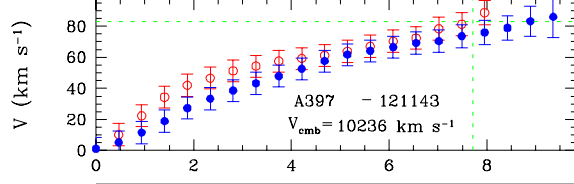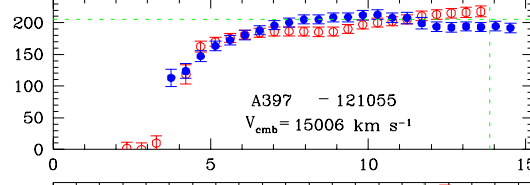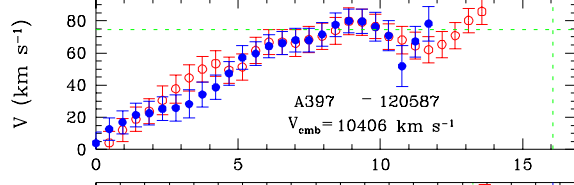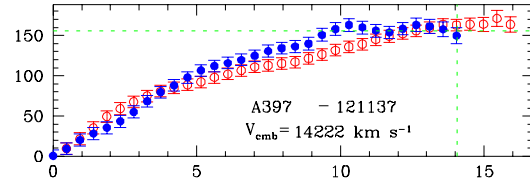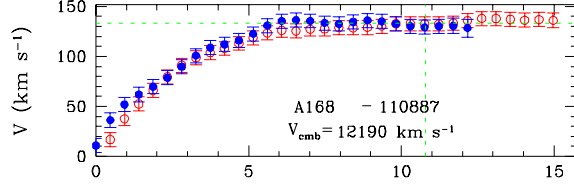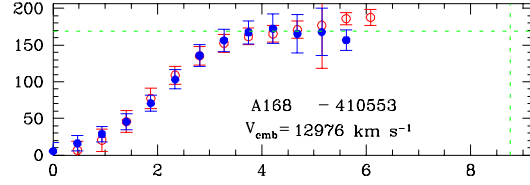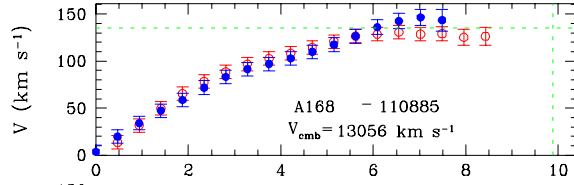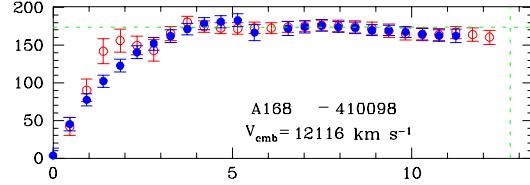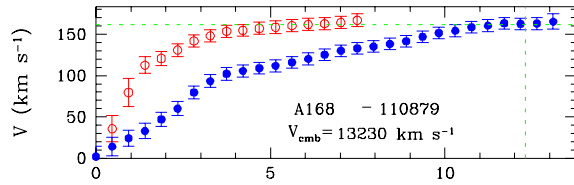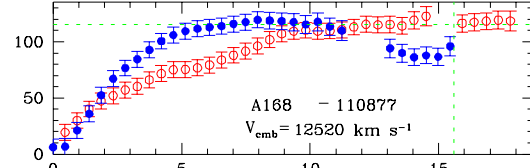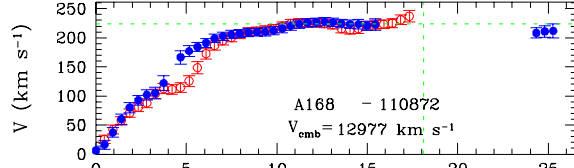
Radius (arcseconds)

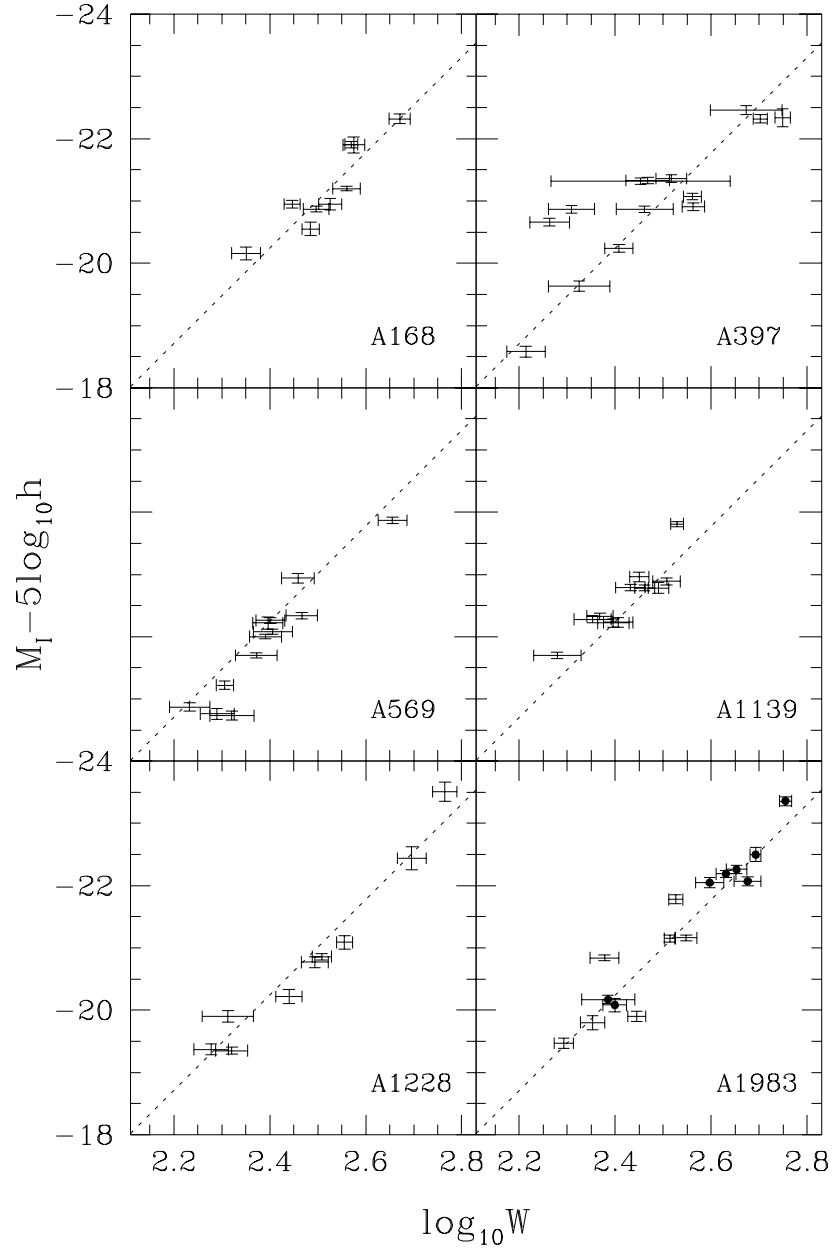fig. 8

Seeking the Local Convergence Depth. I. TF Observations of the Clusters A168, A397, A569, A1139, A1228, and A1983

Daniel A. Dale[1], Riccardo Giovanelli, Martha P. Haynes, Marco Scodeggio[2]

Center for Radiophysics and Space Research and National Astronomy and Ionosphere Center[3], Cornell University, Ithaca, NY 14853

dale,riccardo,haynes,scodeggi@astrosun.tn.cornell.edu

Eduardo Hardy

Department of Physics, Laval University, Ste–Foy, P.Q., Canada G1K 7P4

hardy@phy.ulaval.ca

Luis E. Campusano

Observatorio Astronómico Cerro Calán, Departamento de Astronomía, Universidad de Chile, Casilla 36-D, Santiago, Chile

lcampusa@das.uchile.cl

ABSTRACT

We present first results of an all-sky observing program designed to improve the quality of the I band Tully-Fisher (TF) template and to obtain the reflex motion of the Local Group with respect to clusters to $z \sim 0.06$. We are obtaining between 5 and 15 TF measurements per cluster on a sample of ~ 50 clusters at intermediate redshifts ($0.02 \lesssim z \lesssim 0.06$). Presentation of the data for seven Abell clusters of galaxies is given here. This data incorporates methods for estimating the true inclination of a spiral disk, an observational parameter undervalued for small angular-sized galaxies or for galaxies observed in poor seeing conditions.

Subject headings: galaxies: distances and redshifts – cosmology: observations; distance scale

---

[1]Department of Physics, Cornell University

[2]Now at European Southern Observatory, Karl Schwarzschild Str. 2, D–85748 Garching b. München, Germany

1. Introduction

Claims of large amplitude, coherent flows on scales up to $100h^{-1}$ Mpc (Lauer & Postman 1994:LP; Courteau *et al.* 1993) are difficult to accomodate with current cosmological scenarios (Gramann *et al.* 1995). Observationally, the LP claim has been challenged by several groups (*e.g.* Riess *et al.* 1995 and Giovanelli *et al.* 1996:G96), but a clear–cut solution of the disagreement is still wanting, because the sample of supernova type Ia of Riess *et al.* (1995) is too sparse (Watkins & Feldman 1995) and the Tully–Fisher (TF) sample of G96 is of limited depth. The G96 sample of peculiar velocities ($V_{\rm pec}$'s) obtained using the TF method is referred to a template relation based on 555 galaxies in 24 clusters to $cz \simeq 9000$ km s^{-1} (Giovanelli *et al.* 1997a,b:G97a,b). If the $V_{\rm pec}$ field is characterized by strong spatial gradients, a shallow sample would not provide a quantitatively effective test of large–scale flows. This is particularly important in view of the claims (Scaramella *et al.* 1994, Tini–Brunozzi *et al.* 1995, and Branchini *et al.* 1996) that asymptotic convergence of the Local Group reflex motion may only be reached at distances in excess of 10,000 km s^{-1}. This is the first of a series of papers that aim at the direct determination of the TF relation for an all–sky cluster set extending to distances exceeding the highest reported values of the convergence depth.

A second issue of concern regards the amplitude of systematic errors in the TF template relation used to measure $V_{\rm pec}$. Though the proximity of the G97a,b sample provides the stretch in galactic properties necessary to determine accurately the TF slope, it conversely works against pinning down the relation's zero point offset; peculiar velocities introduce relative distortions of redshifts that are larger for nearby galaxies than for distant ones. Thus, the benefits of measuring peculiar velocities at higher redshifts are twofold: the contribution to the Local Group velocity field arising at large scales is better understood *and* the (offset) accuracy of all $V_{\rm pec}$ measurements improves.

We are complementing the sample of G97a,b by obtaining between 5 and 15 TF measurements in each of approximately 50 clusters with 6000 km s$^{-1} \lesssim cz \lesssim 18{,}000$ km s^{-1}. Explicitly, the goals for this project are to obtain (a) a high quality template TF relation to which local motions can be accurately referred, and (b) a bulk flow dipole solution for a volume of radius 18,000 km s^{-1}.

In order to make the data publicly available on the shortest possible time scale we shall present partial results of our survey, as we complete data analysis for sizable fractions of the cluster set. In this paper we present the project's first data installment: TF measurements for 84 galaxies in the fields of six Abell clusters, one of which, A1983, we actually treat as two separate clusters (see section 6). In addition, we discuss and illustrate with examples some of the systematic effects involved in deriving true TF templates. The following section

details the selection of clusters and galaxies for this project. We describe the imaging of the clusters in section 3 and the optical spectroscopy of the galaxies in section 4. In Section 5 we review the method used to estimate actual disk inclinations from the observed, seeing-distorted inclinations. Section 6 presents the relevant TF data.

2. Selection of Clusters and Galaxies

Clusters are selected using the Abell *et al.* (1989, hereinafter ACO) rich cluster catalog. Details on the selection of the cluster sample will be provided in a separate paper. To determine locations of target fields to be imaged, we visually scanned the Palomar Observatory Sky Survey plates for regions in the clusters containing promising disk systems appropriate for TF work.

The selection of target galaxies for this study stems directly from the images obtained. Each image in clusters chosen for spectroscopy is searched for spiral disks with the following properties: inclinations $\gtrsim 40°$; lack of dominating bulges – bulgy disk systems tend to be gas deficient and thus undesirable for spectroscopy; no apparent warps/interacting neighbors; and no nearby bright stars which may affect flux measurements. Coordinates and position angles for these objects are obtained from the Digitized Sky Survey[4] and are accurate to $<$ $2''$.

Finally, we have earmarked at least two clusters in each semester to be observed from both hemispheres. In this way any systematic differences between data taken in the North and South and between data taken from season to season can be quantified. Preliminary results indicate negligible differences; a detailed analysis will be presented when the bulk of the data has been obtained.

3. Imaging

CCD images of the clusters were obtained at the KPNO and CTIO 0.9 m telescopes. This installment only contains KPNO data observed during the nights of October 5–16 1994, September 14–21 1995, September 24–October 1 1995, and February 13–19 1996. Images were taken in the I band to match the observations of the nearby study of G97a,b and for

---

the reasons outlined therein. The 2048^2 T2KA CCD ($0.68''$ pixel^{-1}) used at the KPNO 0.9 m allows $23'$ fields. Besides being useful in mapping out cluster fields efficiently, such wide fields also help to provide sufficient area in which to determine the sky background. A 600 second integration time was typically used for each exposure; integrating for ten minutes probes the low surface brightness edges (~ 24.5 mag arcsec^{-2}) of galaxies adequately and is generally not long enough to produce saturated galactic cores.

3.1. Photometry Data Reduction

We have made an effort to employ a method of data reduction consistent with the G97 reductions, which will be discussed in Haynes *et al.*, in preparation. Here we summarize those details. Both standard and customized IRAF[5] packages are used. Among the most crucial reduction tasks is obtaining adequately "flat" images due to the increased sky fluctuations present in the infrared, relative to the optical bands. As such, we create flat–field templates by median–combining at least 30 frames that are free from relatively bright stars and relatively large galaxies. Once flat–fielded, each galaxy frame is background corrected by subtracting off the mean value of several sky regions near the galaxy that are free from stars or significant cosmic ray hits (this is done separately for each galaxy). The uncertainty in the sky background is less than 0.2%. Moreover, cosmic rays and also any stars near the galaxy are masked to prevent distortions of the ensuing isophotal ellipse fitting, a procedure that interpolates over masked regions.

The procedure of ellipse fitting employs the GALPHOT surface photometry package written for IRAF/STSDAS[6] by W. Freudling, J. Salzer, and M.P. Haynes. We fit ellipses to increasing galactic radii until the background is reached. The bulk of the instrumental magnitude is determined from data within the outermost isophote, but a small yet non–zero contribution, found by extrapolating the "curve of growth" of the surface magnitude of each spiral galaxy to infinity (assuming the light drops like that of an exponential disk), is also included (see G94 for details on this procedure) to infer a "total" magnitude, m$_\infty$. This contribution is typically a few hundredths of a magnitude. In this paper we also report the values of the isophotal magnitude, $m_{23.5}$, measured at the 23.5 mag arcsec^{-2} isophote.

---

[5]IRAF (Image Reduction and Analysis Facility) is distributed by the National Optical Astronomy Observatories, which are operated by the Association of Universities for Research in Astronomy, Inc. (AURA), under a cooperative agreement with the National Science Foundation.

[6]STSDAS (Space Telescope Science Data Analysis System) is distributed by the Space Telescope Science Institute, which is operated by AURA, under contract to the National Aeronautics and Space Administration.

Errors on $m_{23.5}$ and m_∞ typically hover between 0.02 and 0.04 mag – the corrections for internal extinction introduce further uncertainty, as discussed in the next section.

Instrumental magnitudes are converted to apparent magnitudes using Landolt (1992) standard stars. Many observations of standards were made each night in the R and I bands to cover a broad stretch in both airmass and R-I color. We find a small dependence on airmass (~ 0.1 mag airmass^{-1}) and a negligible color effect. This is fortunate since we only have I band images; assuming an R-I galactic color of 0.5 mag yields negligible color corrections. Finally, we emphasize that only data taken on nights where the photometric zero point is determined to 0.02 mag or better are used.

The ellipse fitting is also important in determining the ellipticity of the disk and hence inferring its inclination. We discuss in detail the process of determining "true" disk inclinations in section 5.

3.2.   Corrections to I Band Magnitudes

We use Burstein and Heiles' (1978) method for tabulating galactic extinction values by averaging entries in the *Third Reference Catalogue of Bright Galaxies* (de Vaucouleurs *et al.* 1991) found near the cluster centers. We convert B-Band extinctions to I band via $A_I = 0.45 A_B$; values of A_I for the seven clusters presented here range from 0.00 to 0.18 mag. The internal extinction correction is applied using the procedure outlined in G97a, whereby the decrease in apparent luminosity of late-type galaxies due to their dusty disks can be quantified as

$$\Delta m_{\mathrm{int}} = -f(T)\,\gamma(W_{\mathrm{cor}})\,log(1-e) \tag{1}$$

where γ ($\lesssim 1.0$) depends on the corrected velocity width W_{cor} (section 4.3) and e is the ellipticity of the spiral disk (the correction Δm_{int} is slightly smaller for early, less dusty gals: $f(T)$=0.85 for types T earlier than Sbc; $f(T)$=1 otherwise). In other words, the internal extinction depends on the size of the system and on how inclined the disk is to our line of sight. An error for γ of 0.15γ is assumed. We apply a cosmological k–correction: $k_I = (0.5876 - 0.1658T)z$ (Han 1992). Finally, we are careful to apply a small correction, Δm_T, for the TF dependence on morphological type found in G97b. Thus, the apparent magnitudes given in this paper are

$$m_{\mathrm{cor}} = m_\infty - A_I - k_I - \Delta m_{\mathrm{int}} - \Delta m_T. \tag{2}$$

Note that A_I, Δm_{int}, and Δm_T are all positive quantities in equation (2).

4. Spectroscopy

Though the 21 cm spectral line is a frequently adopted tool in TF work — the HI distribution in galaxies typically extends further out than that of HII regions and thus samples rotation curves at larger radii — the characteristics of our sample favor the use of optical spectroscopy. Too few radio telescopes exist with the sufficient sensitivity, spatial and velocity resolution, and bandwidth necessary for an all–sky survey of intermediate distance clusters. The dishes at Nançay and Arecibo would be useful, but cannot cover the whole sky. In cluster fields at $cz \gtrsim 10^4$ km s^{-1}, confusion becomes a problem and, especially at Arecibo, the interference environment makes observations more difficult. Array instruments still have limited correlator power to cover the large bandwidth required for cluster observations with sufficient resolution. Furthermore, many cluster spirals are HI deficient (Giovanelli & Haynes 1985). For these reasons we have chosen to adopt emission line spectroscopy near the Hα line to measure velocity widths; we detected Hα emission in 91 out of 105 targeted galaxies observed in these seven clusters. The spectroscopy was carried out at the Palomar Observatory 5 m telescope over the course of four observing runs. The nights of observing included: October 22–23 1995, December 13–18 1995, Jan 24–25 1996, and May 14–15 1996.

For this project we used the red camera (5200 – 11,000 Å) of the Double Spectrograph (Oke and Gunn 1982) at the Cassegrain focus ($f/15.7$). The combination of the 1200 lines mm^{-1} grating and a 2$''$ wide slit yields a dispersion of 0.65 Å pixel^{-1} and a spectral resolution of 1.7 Å (equivalent to 75 km s^{-1} at 6800 Å). Along the cross–dispersion axis, the spatial scale is 0.46$''$ pixel^{-1}. Since we are interested in observing cluster members with redshift velocities of up to $\sim$ 25,000 km s^{-1}, the angle of the grating is set in order to observe the Hα line at wavelengths anywhere between 6560 Å ($\sim$ rest wavelength) and 7230 Å ($cz \sim$ 30,000 km s^{-1}).

As an observing strategy, we perform a five minute test integration on each spectroscopic target. In this way we are able to determine "on the fly" the requisite exposure time to adequately sample the outer disk regions. Furthermore, this test exposure determines if the galaxy is even useful to our work; the galaxy may lie in the foreground or background of the cluster or it may contain little or no Hα emission. If the observation is deemed useful, a second integration typically ranges between 15 and 45 minutes.

4.1. Spectroscopy Data Reduction

Standard and customized IRAF tasks are used in reducing the spectroscopic data. The spectra are wavelength calibrated using both night sky lines and HeNeAr comparison lamps. The residual uncertainties in the spectral calibration translate to a typical velocity uncertainty of ~ 7 km s^{-1}, a figure which is added in quadrature to the errors from the rotation curve fitting (below) in determining the total error for each data point. The night skylines and the galactic continuum are fit with polynomials and then subtracted from the spectra. Finally, the Hα rotation curve is computed. In $\sim 1\%$ of the cases the emission of a N[II] line (6584 Å) is stronger and extends to larger radii than that of the Hα emission; in these cases the N[II] curve is used. At each position along the cross–dispersion axis we fit a Gaussian profile to the light distribution (averaged over three pixels in the spatial direction). The position of the Gaussian peak is taken to be the line centroid for that spatial location. Since the seeing is typically $1''$ to $2''$, the rotation curves are oversampled by a factor of two to three. The galactic center-of-light is defined to be at the peak of the galaxy continuum light profile formed by summing the data along the dispersion direction.

4.2. Calculating Systemic Velocities and Velocity Widths

It is necessary to extract two parameters from each rotation curve: the systemic velocity (*i.e.* redshift) and the Doppler velocity width. In an idealized galaxy, where both arms of the rotation curve are smoothly traced out beyond the turnover radius, the two velocity extrema are all that are needed – the average of the extrema is the systemic velocity and the difference is the velocity width. Unfortunately, rotation curves can exhibit erratic behavior. To determine velocity widths, we sort the velocity data points and calculate the difference between the 10% and 90% velocities (An N% velocity is greater than N% of all the velocity data points). This technique is effectively a "pixel histogram," similar in flavor to the portrayal of raw 21 cm data.

The systemic and rotational velocity extracted from an observed rotation curve depends on whether a photometric or kinematic center of symmetry is assumed. In the first case, the systemic velocity is assigned the value at the location where the galaxy light peaks. In the upper panel of figure 1, the rotation curve is folded about such a photometric center, exhibiting asymmetry in the outer parts. Alternatively, by forcing a match between the asymptotic rotational velocity in the outer parts of the galaxy, a "kinematical centering" can be obtained. This kinematic center is merely the average of the 10% and 90% velocitites. In the lower panel of figure 1, the rotation curve of the same galaxy in the upper panel is folded about the kinematic center, which is shifted from the photometric center by $0.92''$.

The systemic velocity differs by 34 km s^{-1} between the two cases. In what follows, we will adopt the kinematical centering technique.

4.3.   Corrections to Velocity Widths

Besides avoiding the spatial confusion problem encountered by single dish radio telescopes, important in observing galaxies clustered together at intermediate redshifts, optical emission line spectroscopy provides detailed mapping of the rotation curve along the chosen position angle. This mapping facilitates estimating the impact of the optical rotation curve (ORC) shape (*e.g.* still rising at the optical radius) on the determination of the velocity width. On the other hand, advantages of using the 21 cm line include that 1), velocity widths are "position angle–independent" and 2), HI typically extends farther than the optical radius; an HI velocity width is more likely to have included light near or beyond the turnover radius, the point at which the rotation curve begins to fall. Hence, in many instances, 21 cm work gives more accurate velocity widths than could be measured optically. Haynes *et al.* (1997) reports 21 cm measurements for ~ 840 galaxies at redshifts of up to $z \sim 0.04$, a data set which has a small overlap with our sample; we forego Hα and use 21 cm widths when they are available (see Table 2).

The first correction applied to the observed velocity width, $W_{\rm obs}$, is an additive term $\Delta_{\rm sh}$ that depends on the radial extent and shape of the ORC. Small corrections are applied to the velocity widths in cases when the ORC does not extend to $R_{\rm opt}$, the distance along the major axis to the isophote containing 83% of the I band flux. This is reported by Persic & Salucci (1991 & 1995) to be a useful radius at which to measure the velocity width of ORCs. The value of $\Delta_{\rm sh}$ is larger for non-asymptotic ORCs, but is usually less than 10% of the velocity width; it is estimated by fitting a "universal rotation curve" function to the data as advocated by Persic & Salucci, and extrapolating it to $R_{\rm opt}$. We remark that this application of the Persic & Salucci formalism is merely a tool for a mild extrapolation of the outer part of the rotation curve for the estimation of uncertainties, and is not a test of the relation's universality. It should be noted that we do not use galaxies whose rotation curves are still rising significantly at the end of the Hα distribution (*e.g.* curves exhibiting only solid–body rotation are deemed unusable for TF work). The other corrections to the observed velocity width are the factors $1/(1+z)$ and $1/\sin i$, the first of which accounts for the cosmological broadening of rotation curves and the second corrects for the inclination i at which a given disk is observed. The corrected optical velocity width can be expressed as

$$W_{\rm cor} = \frac{W_{\rm obs} + \Delta_{\rm sh}}{(1+z)\sin i}. \tag{3}$$

4.4. Errors in Velocity Widths

Many factors contribute to the uncertainty in a velocity width measurement, including the inclination i. In practice we measure a disk's ellipticity, ϵ, so to describe inclinations in terms of ellipticities, we follow Hubble (1926) in assuming spiral disks are oblate spheroids with intrinsic axial ratio q:

$$\cos^2 i = \frac{(1-\epsilon)^2 - q^2}{1 - q^2}.$$ (4)

We also follow the convention outlined in Giovanelli et $al.$ (1994;G94) in adopting a value of q=0.13 for type Sbc and later and a value of q=0.2 for morphological types earlier than Sbc. Formally, the error in the inclination i can be expressed as

$$\sigma_i^2 = \left(\frac{di}{d\epsilon}\right)^2 \sigma_\epsilon^2 + \left(\frac{di}{dq}\right)^2 \sigma_q^2$$ (5)

where σ_ϵ is the uncertainty in the disk ellipticity measurement and σ_q is the error in q, assumed to be $0.15q$.

We can now quantify the error in the velocity width:

$$\sigma_w^2 = \frac{\sigma_{w,\mathrm{obs}}^2 + \sigma_{\mathrm{sh}}^2}{(1+z)^2 \sin^2 i} + \sigma_i^2 W_{\mathrm{cor}}^2 \cot^2 i$$ (6)

where $\sigma_{w,\mathrm{obs}}$ is the error in the observed velocity width and σ_{sh} is the error in the shape correction applied, typically $0.25\Delta_{\mathrm{sh}}$. In the few cases where a 21 cm width is used, we follow G97a in computing errors in the widths.

5. Inclination Corrections

Knowledge of the true rotational velocity widths of galaxies is crucial to TF studies, yet many circumstances combine to yield incorrect measurements. Among these circumstances in optical spectroscopy work are misalignment of the slit with the major axis of the galaxies and insufficient integration times that prevent unambiguous measurements in the outer parts of the ORC. The largest error contributed to estimates of the velocity width in general derives from uncertainty in the angle of inclination, i, of the disk to the line of sight. As described in the previous section, this geometric effect can be easily accounted for by dividing the observed velocity width by $\sin i$. In addition, a knowledge of the correct ellipticity of a disk is important in the derivation of the internal extinction correction to the total magnitude, as discussed in section 3.2. It is the ability to correctly measure the ellipticity that we are concerned with here.

It is well–known that ground-based observations are affected by the atmospheric seeing conditions. Saglia *et al.* (1993;S93) have recently provided a thorough analysis concerning the effects of seeing on spheroidal systems. The turbulent atmosphere increasingly affects the observed ellipticities, $\epsilon_{\rm obs}$, as the angular size of galaxies decreases. Here we consider that effect on spiral disks.

5.1. Measuring True Ellipticities

In order to gauge the relationship between $\epsilon_{\rm obs}$ and the undistorted ellipticity $\epsilon_{\rm true}$, we have taken a sample of eleven large angular–sized galaxies (major axis $> 5'$) with a broad range of inclinations and bulge–to–disk ratios and blurred their (I band) images by convolving them with a point spread function (psf) of varying width. The galaxies used in this exercise are a mix of Sa and Sc type galaxies and had $\epsilon_{\rm true}$ ranging between 0.311 and 0.865 and bulge–to–disk ratios between 0 and 2. We assume that the unconvolved images yield $\epsilon_{\rm true}$.

It is necessary in this exercise to mimic the actual seeing profile as closely as possible. Though the seeing quality for an observation is typically conveyed by measuring the FWHM of a Gaussian fit to a stellar profile, it is known that stellar profiles do not drop as steeply outside of their cores as Gaussians do (Woolf 1982). To simulate this effect we have followed the method of S93 which employs atmospheric turbulence theory and empirical results to predict the stellar psf and its parameters. Letting the stellar psf be $p_\gamma(r)$, it can be shown that

$$p_\gamma(r) = \frac{1}{2\pi}\int_0^\infty dk \; k \; e^{-(kb)^\gamma} J_0(kr), \quad \gamma = 5/3 \tag{7}$$

where r is the radial distance, J_0 is the standard Bessel function, b is FWHM/2.921, and γ is a parameter predicted to be 5/3 by theory.

For a fixed $\epsilon_{\rm true}$, we expect $\epsilon_{\rm true}/\epsilon_{\rm obs}$ to increase when either the size of the seeing disk increases or the angular size of the galaxy decreases. We have thus parametrized the change in ellipticity as a function of the ratio between the measured seeing FWHM and the face–on disk scale length, $R_{\rm d}^\circ$ (see G94 for details on measuring $R_{\rm d}^\circ$). We thus define

$$\eta \equiv \frac{\rm FWHM}{R_d{}^\circ}. \tag{8}$$

We have convolved each galaxy image with a range of values for η and measured the resulting ellipticities. Figure 2 gives our results for the eleven galaxies used in this study, plotting $\epsilon_{\rm true}/\epsilon_{\rm obs}$ as a function of η. We find that, within the uncertainties of our simulations, the change in the ratio $\epsilon_{\rm true}/\epsilon_{\rm obs}$ is independent of disk inclination and

bulge–to–disk ratio. Fitting a linear relation to the data gives us a general method for estimating ϵ_{true} as a function of the observable quantities ϵ_{obs}, FWHM, and $R_{\text{d}}{}^{\circ}$. We see that the change in ellipticity is not severe; there is only a $\sim 10\%$ difference even for $\eta \sim 1$, the extreme case when the seeing is comparable to the disk scale length. More exactly,

$$\epsilon_{true} = \epsilon_{obs} + 0.118\,\eta\,\epsilon_{obs} \tag{9}$$

where the 1-σ errors in the offset and slope are 0.004 and 0.011, respectively.

5.2. Examples of the Impact of Inclination Corrections

As mentioned previously, both the velocity width and the total magnitude depend on the disk inclination. Quantitative examples of the corrections applied are useful to get a feeling as to how TF parameters are changed. Suppose two Sc galaxies with total velocity widths of 300 km s^{-1} are observed, with one inclined to the line of sight at 85.0° (galaxy 'A') and the other at an inclination of 48.0° (galaxy 'B'). This means the projected velocity widths would be 299 km s^{-1} and 223 km s^{-1} respectively for galaxies A and B (ignoring cosmological effects). Furthermore, suppose the sizes of the galaxies and the seeing conditions yield $\eta = 1.00$ in each case (an extreme value of η is chosen to understand what the magnitudes of the largest probable corrections would be). Thus, according to equations (4) and (9), though galaxy A has a true disk ellipticity of 0.844 it will be observed to have an ellipticity of 0.755 ($i = 77.9°$). Similarly, galaxy B has $\epsilon_{\text{true}} = 0.324$ but $\epsilon_{\text{obs}} = 0.290$ ($i = 45.2°$). We see that without accounting for the circularizing effect atmospheric seeing has on these disks, one would incorrectly infer the velocity widths for galaxies A and B to be 306 km s^{-1} and 314 km s^{-1} instead of the actual 300 km s^{-1}.

Seeing also affects the correction for internal extinction. According to equation (1), galaxy A "should" have a correction of 0.742 mag and galaxy B, 0.156 mag, but the observed axial ratios would imply corrections of only 0.562 and 0.137 mag.

This simple example highlights how seeing affects differently oriented disks. Without making the proper corrections for seeing, galaxies that are highly inclined would yield reasonable velocity widths but the internal extinction corrections for the galaxies would be uncomfortably awry. Conversely, galaxies considered to be borderline TF candidates due to their low inclinations are not affected greatly by miscalculating the internal extinction, but errors in determining the inclinations would produce velocity width errors of $\sim 5\%$.

6. Data

We present here the relevant data for the first set of seven Abell clusters, including 84 galaxies for which we have obtained both photometric parameters and rotational velocity widths. We classify 70 of these galaxies to be cluster members with good widths; 15 galaxies are foreground or background objects or are cluster members with poorly defined velocity widths.

Table 1 lists the main parameters of the clusters. Standard names are listed in column 1. Adopted coordinates of the cluster center are listed in columns 2 and 3, for the epoch 1950; they are obtained from ACO, except for the entry A1983b, a system found to be slightly offset from A1983 in both sky position and redshift. For all the clusters we derived a new systemic velocity, combining the redshift measurements available in the NED[7] database with our own measurements. These newly determined velocities are listed in columns 4 and 5, in the heliocentric and in the CMB (Kogut *et al.* 1993) reference frame, respectively. We list the number of cluster member redshifts used in determining systemic velocities in column 6. An estimated error for the systemic velocity is parenthesized after the heliocentric figure. Spherical and Cartesian supergalactic coordinates are given in columns 7 and 8, and in columns 9–11, respectively.

Figures 3–5 show the distribution of the galaxies in each cluster. The top panel in each of these figures displays the spatial location of: the outline of the fields imaged (large squares), cluster members (circles – those with poor/unusable velocity widths are left unfilled), background or foreground objects (asterisks), and galaxies with known redshift but without reliable widths (dots). Circles of 1 and 2 Abell radii, R_A, are drawn as dashed lines, if the area displayed is large enough. If no dashed circle is drawn, R_A is larger than the figure limits. We also plot radial (CMB) velocity as a function of angular distance from the cluster center in the lower panel of each figure. A dashed vertical line is drawn at 1 R_A. The combination of the sky and velocity plots is used to gauge cluster membership for each galaxy. We point out that each of the filled circles do indeed identify *bona fide* cluster members – all but two of the galaxies we label as cluster members lie within 1 R_A and all cluster members are within 1300 km s^{-1} of the cluster systemic radial velocity.

We separate photometric data and spectroscopic data in two tables. Table 2 lists the spectroscopic properties and table 3 gives the pertinent photometric results.

Entries in the tables are sorted first by the Right Ascension of each cluster, and within

---

each cluster sample by increasing galaxy Right Ascension. The listed parameters for table 2 are:

Col 1: identification names corresponding to a coding number in our private database, referred to as the Arecibo General Catalog, which we maintain for easy reference in case readers may request additional information on the object.

Cols. 2 and 3: Right Ascension and Declination in the 1950.0 epoch. Coordinates have been obtained from the Digitized Sky Survey catalog and are accurate to $< 2''$.

Cols. 4 and 5: the galaxy radial velocity as measured in the heliocentric and CMB reference frame (Kogut *et al.* 1993). Errors are parenthesized: *e.g.* 13241(08) implies 13241±08.

Col. 6: the raw velocity width in km s^{-1}. Measurement of optical widths are described in section 4; 21 cm line widths are denoted with a dagger and refer to values measured at a level of 50% of the profile horns.

Col. 7: the velocity width in km s^{-1} after correcting for ORC shape and, for 21 cm data, signal to noise effects, insterstellar medium turbulence, and instrumental and data processing broadening; details on the adopted corrections for optical and 21 cm data are given in section 4 and G97a, respectively.

Col. 8: the corrected velocity width converted to edge–on viewing, in km s^{-1}, after accounting for the cosmological stretch of the data.

Col. 9: the adopted inclination i of the plane of the disk to the line of sight, in degrees, (90° corresponding to edge–on perspective); the derivation of i and its associated uncertainty are discussed in section 4.

Col. 10: the logarithm in base 10 of the corrected velocity width (value in column 7), together with its estimated uncertainty between brackets. The uncertainty takes into account both measurement errors and uncertainties arising from the corrections. The format 2.576(22), for example, is equivalent to 2.576±0.022.

The position angle adopted for the slit of each spectroscopic observation is that given in column 4 of table 3. The first column in table 3 matches that of table 2. The remaining listed parameters for table 3 are:

Col. 2: morphological type code in the RC3 scheme, where code 1 corresponds to Sa's, code 3 to Sb's, code 5 to Sc's and so on. When the type code is followed by a "B", the galaxy disk has an identifiable bar. We assign these codes after visually inspecting the CCD I band images and after noting the value of R_{75}/R_{25}, where R_X is the radius containing X% of the I band flux. This ratio is a measure of the central concentration of the flux which was

computed for a variety of bulge–to–disk ratios. Given the limited resolution of the images, some of the inferred types are rather uncertain.

Col. 3: the angular distance θ in arcminutes from the center of each cluster.

Col. 4: position angle of the major axis of the image, also used for spectrograph slit positioning (North: 0°, East: 90°).

Col. 5: observed ellipticity of the disk.

Col. 6: ellipticity corrected for seeing effects as described in section 5, along with its corresponding uncertainty. The format 0.780(16), for example, is equivalent to 0.780±0.016.

Col. 7: surface brightness at zero radius, as extrapolated from the fit to the disk surface brightness profile.

Col. 8: the (exponential) disk scale length.

Col. 9: the distance along the major axis to the isophote containing 83% of the I band flux.

Col. 10: isophotal radius along the major axis where the surface brightness equals 23.5 mag sec^{-2}.

Col. 11: apparent magnitude within the 23.5 mag sec^{-2} isophote.

Col. 12: the measured I band magnitude, extrapolated to infinity assuming that the surface brightness profile of the disk is well described by an exponential function.

Col. 13: the apparent magnitude, to which k–term, galactic and internal extinction corrections were applied; details on the adopted corrections are given in section 3.

Col. 14: the absolute magnitude, computed assuming that the galaxy is at the distance indicated either by the cluster redshift, if the galaxy is a cluster member, or by the galaxy redshift if not. The calculation assumes $H_\mathrm{o} = 100h$ km s^{-1}Mpc^{-1}, so the value listed is strictly $M_\mathrm{cor} - 5 \log h$. In calculating this parameter, radial velocities are expressed in the CMB frame and uncorrected for any cluster peculiar motion. The uncertainty on the magnitude, indicated between brackets in hundredths of a mag, is the sum in quadrature of the measurement errors and the estimate of the uncertainty in the corrections applied to the measured parameter.

When an asterisk appears at the end of the record, a detailed comment is given for that particular object. Because of the length and number of these comments, they are not appended to the table but included in the text as follows. Note that a record is flagged in both tables 2 and 3, independently on whether the comments refer only to the photometry,

only to the spectroscopy, or both.

A168:

110868: HII distribution patchy and does not extend far radially; exponential disk over narrow range of radii.

110877: asymm. ORC.

110879: asymm. central region, both in image and ORC; difficult to determine ellipticity.

410553: mostly bulge ORC; tiny gal.

A397:

121137: background gal.

120587: prob. used incorrect PA; 21 cm width preferred; note low i.

121055: background gal.

121143: tiny gal; ORC still rising at optical radius; poorly determined 21 cm width.

121145: background gal.

121060: background gal.

121061: background gal.

2406: patchy HII; good agreement between 21 cm and ORC width; used N[II] ORC.

120614: only 21 cm width available; note early type; unfit for TF use.

121154: mostly bulge ORC; uncertain vel. width.

121157: background gal.

120632: poor HII sampling; 21 cm width available

2420: asymm. HII distrib.; compatible ORC and 21 cm widths.

120651: asymmetric ORC; PA uncert.; 21 cm width used.

120652: Hα absorption in bulge; note low i; good agreement between 21 cm and ORC width.

121080: note low i.; compatible 21 cm and ORC widths.

121082: only 21 cm width available; caution: nearby star may perturb phot.

121085: patchy HII; uncertain PA.

2453: uncertain ellipticity; Hα absorption in bulge; $W_{ORC} = 360$ km s^{-1}; 21 cm width available.

A569:

170433: ORC still rising.

170437: background gal.

170438: ORC only from bulge.

170439: ORC still rising?

140440: note low i.

170442: ORC slightly rising.

170446: exponential disk over small range of radii.

170057: ORC slightly rising.

3724: only 21 cm width available.

170063: Sd or irregular morphology?

170468: background gal.

A1139:

200723: mostly bulge ORC.

200743: mostly bulge ORC.

201069: mostly bulge ORC; uncert. vel. width.

A1228:

6357: only 21 cm width available.

6364: dust lane along major axis; opt. radius signif. larger than ORC's extent; used N[II] ORC.

211475: background gal.

211476: bar distorts ORC; unfit for TF use.

211406: asymm. ORC; tiny disk.

A1983:

241306: only 21 cm width available.

240823: only 21 cm width availablle.

240840: mostly bulge ORC.

241298: weak, patchy HII distrib, but ORC fine.

A1983b:

241056: background gal.; not used in fits.

9538: unreliable ORC; severe Hα absorption; 21 cm width available.

241059: only 21 cm width available.

241061: background gal.; Hα partially absorbed and λ6548 completely absorbed!.

241296: large extrapolation to ORC.

240746: only 21 cm width available.

240747: 21 cm width available; interacting w/faint companion? prob. unfit for TF use.

9548: low vel. horn in 21 cm data poorly defined.

9550: compatible ORC and 21 cm widths.

In figure 6, we plot the ORCs folded about a kinematic center as described in section 4. The horizontal dashed line in each panel indicates the adopted (and uncorrected for inclination) half velocity width, $W/2$, for each galaxy and the vertical dashed line is drawn at $R_{\rm opt}$. Finally, in figure 7 we give, as an example, the surface brightness profiles for the first 16 galaxies in figure 6. Again the vertical dashed line refers to $R_{\rm opt}$. The solid line drawn along the disk is the fit to the disk over the range of radii assumed to cover the exponential portion of the disk. The remainder of the plots of surface brightness profiles for the complete sample can be obtained by contacting the first author.

Figure 8 gives the "raw" TF plots of each cluster uncorrected for any cluster incompleteness bias. A computation of such bias will be presented in future work when data

from all clusters is in hand. Furthermore, the cluster systemic redshifts used in obtaining these plots are preliminary. A given cluster's systemic velocity is inferred from all available redshifts in its field. While we have tried to target clusters with a broad redshift database (or for which redshift surveys are ongoing, as we have learned from informal contacts with colleagues), the definition of a cluster's $<cz>$ will be of variable quality. The peculiar velocity inferred from the TF relation will be affected by this uncertainty. The exact amplitude of that uncertainty will be estimated when all the redshift data will become available, at the completion of this study. *Thus the TF relations presented in figure 8 are to be considered preliminary.* Included in the TF plots is the template relation obtained from nearby clusters in G97b:

$$y = -7.68x - 21.01 \tag{10}$$

where y is $M_{cor} - 5\log h$ and x is $\log W_{cor} - 2.5$.

REFERENCES

Abell, G., Corwin, H.G. and Olowin, R.P. 1989, ApJS 70, 1 [ACO]

Branchini, E., Plionis, M. and Sciama, D.W. 1996, ApJ 461, L17

Burstein, D. and Heiles, C. 1978, ApJ 225, 40

Courteau, S., Faber, S., Dressler, A. and Willick, J. 1993, ApJ 412, L51

de Vaucouleurs, G., de Vaucouleurs, A., Corwin, H.G., Buta, R.J., Paturel, G., and Fouqué, P. 1991. *Third Reference Catalogue of Bright Galaxies.* New York: Springer

Giovanelli, R. and Haynes, M.P. 1985, ApJ 292, 404

Giovanelli, R., Haynes, M.P., Salzer, J J., Wegner, G., Da Costa, L.N. and Freudling, W. 1994, AJ 107, 2036

Giovanelli, R., Haynes, M.P., Wegner, G., da Costa, L.N., Freudling, W. and Salzer, J.J. 1996, ApJ 464, L99 [G96]

Giovanelli, R., Haynes, M.P., Herter, T., Vogt, N.P., Wegner, G., Salzer, J.J., da Costa, L.N. and Freudling, W. 1997, AJ 113, 22 [G97a]

Giovanelli, R., Haynes, M.P., Herter, T., Vogt, N.P., da Costa, L.N., Freudling, W., Salzer, J.J. and Wegner, G. 1997, AJ 113, 53 [G97b]

Gramann, M., Bahcall, N.A., Cen, R. and Gott, J.R. 1995, ApJ 441, 449

Han, M. 1992, ApJS 81, 35

Haynes, M., Giovanelli, R., Herter, T., Vogt, N., Freudling, W., Maia, M., Salzer, J. and Wegner, G. 1997, AJ in press.

Hubble, E. 1926, ApJ 64, 321

Kogut, A. *et al.* 1993, ApJ 419, 1

Landolt, A. 1992, AJ 104, 340

Lauer, T. and Postman, M. 1994, ApJ 425, 418

Oke, J.B. and Gunn, J.E. 1982, PASP 94, 586

Persic, M. and Salucci, M. 1991, ApJ 368, 60

Persic, M. and Salucci, M. 1995, ApJS 99, 501

Riess, A., Press, W. and Kirshner, R. 1995, ApJ 445, L91

Saglia, R. P., Bertschinger, E., Baggley, G., Burstein, D., Colless, M., Davies, R.L., McMahan Jr, R.K. and Wegner, G. 1993, MNRAS 264, 961 [S93]

Sandage, A., Binggeli, B. and Tammann, G.A. 1985, AJ 90, 1759

Scaramella, R., Vettolani, G. and Zamorani, G. 1994, ApJ 422, 1

Tini–Brunozzi, P., Borgani, S., Plionis, M., Moscardini, L. and Coles, P. 1995, MNRAS 277, 1210

– 19 –

Tully, R.B. and Fisher, J.R. 1977, A&A 54, 661

Watkins, R. and Feldman, H. 1995, ApJ 453, L73

Woolf, N. J., 1982, ARA&A 20, 367

Fig. 1.— A comparison of folding techniques. The upper panel gives an ORC folded about the galactic *center–of–light* whereas the lower panel displays the ORC folded about the *kinematic* center of the galaxy. The redshift of the galaxy changes by only 34 km s^{-1} and the radii are shifted by only $0.92''$, but the effect is striking. We adopt the lower panel convention.

Fig. 2.— Results of simulations on the effects of seeing on disk ellipticities. η is the ratio of the seeing FWHM to $R_{\mathrm{d}}{}^{\circ}$. Plotted are the data points for simulations carried out on 11 galaxies of differing bulge–to–disk ratios and ellipticities. The "true" ellipticities (as measured from the raw, unconvolved images) of these 11 galaxies are given in the lower right. We use the linear relation drawn to recover "true" ellipticities.

Fig. 3.— Sky and velocity distribution of galaxies in the clusters Abell 168 and Abell 397. Circles represent cluster members with measured photometry and widths; if unfilled, widths are poorly determined. Asterisks identify foreground and background galaxies and dots give the location of galaxies with known redshift, but lacking accurate width and/or photometry. Large square boxes indicate outlines of imaged fields with the 0.9 m telescope. Vertical dashed lines in the lower panels indicate 1 R_{A}. The upper panels contain circles of radius 1 R_{A} (and 2 R_{A} for A168).

Fig. 4.— Sky and velocity distribution of galaxies in the clusters Abell 569 and Abell 1139. Filled circles, unfilled circles, asterisks, dots, large squares and dashed lines and circles follow the same convention as in Figure 3. Note that the upper panel for Abell 569 is smaller than a circle of radius 1 R_{A}.

Fig. 5.— Sky and velocity distribution of galaxies in the clusters Abell 1228, Abell 1983, and Abell 1983b. For A1228 and A1983, filled circles, unfilled circles, asterisks, dots, large squares and dashed lines and circles follow the same convention as in Figure 3. For A1983b, filled triangles identify cluster members and R_{A} is indicated by the dotted line in the lower panel.

Fig. 6.— Hα rotation curves for 76 galaxies (except for galaxies 6364 and 2406, for which the ORC is obtained from a N[II] emission line), folded about the kinematic centers (see figure 1). The error bars include both the uncertainty in the wavelength calibration and the ORC fitting routine used. Names of the galaxy and the corresponding parent cluster are given along with the CMB radial velocity. Two dashed lines are drawn: the horizontal line indicates the adopted half velocity width, W/2, which in some cases arises from an extrapolation to the ORC or from a 21 cm width (see Table 2); the vertical line is at R_{opt}, the radius containing 83% of the I band flux. Note that the rotation curves are *not* deprojected to an edge–on orientation.

Fig. 7.— A sampling of surface brightness profiles. Names of the galaxy and the corresponding parent cluster are given in each panel. Two lines are drawn: the vertical dashed line is drawn at R_{opt} and the solid line is an exponential fit to the disk, over the range of radii over which the disk is assumed to behave exponentially.

Fig. 8.— "Raw" TF plots for the seven clusters are given. We emphasize that the data have *not* been corrected for incompleteness bias. We also note that A397 is seen through a region of the Milky Way with a large and unevenly distributed extinction which leads to increased scatter. In the A1983 panel, the error bars containing filled circles represent members of "A1983b," a cluster at a slightly lower redshift than A1983. The dashed line is the template relation valid for low z clusters, eqn. (10).

TABLE 1. Cluster Coordinates

Cluster	R.A.	Decl.	V_{hel}	V_{cmb}	N_z	SGL	SGB	X	Y	Z
	h m s	d m s	$km\ s^{-1}$	$km\ s^{-1}$		°	°	$km\ s^{-1}$	$km\ s^{-1}$	$km\ s^{-1}$
(1)	(2)	(3)	(4)	(5)	(6)	(7)	(8)	(9)	(10)	(11)
A 168	011234	−000200	13382(69)	13066	43	−62.0	−4.8	6120	−11493	−1088
A 397	025412	+154500	9860(76)	9651	38	−38.0	−23.3	6989	−5454	−3815
A 569	070524	+484200	5948(55)	6032	36	29.0	−25.6	4756	2641	−2606
A1139	105530	+014600	11855(59)	12218	24	106.2	−27.6	−3026	10399	−5656
A1228	111848	+343600	10553(39)	10830	32	76.7	−9.4	2467	10397	−1763
A1983	145024	+165700	13534(46)	13721	76	106.3	32.1	−3255	11162	7285
A1983b	144724	+170600	11328(102)	11521	14	106.0	31.4	−2705	9457	5999